

Effect of Coincident Laser Exposure on Porosity and Tensile Behavior of SS316L Fabricated by Dual-Laser L-PBF

Ishfaqur Rahman¹, Scott Thompson^{2*}

¹Department of Mechanical and Aerospace Engineering, University of Missouri, Columbia, MO 65211, United States of America.

²Department of Mechanical and Aerospace Engineering and University of Missouri Research Reactor (MURR), University of Missouri, Columbia, MO 65211, United States of America.

*Corresponding author: smthompson@missouri.edu

Abstract

The influence of coincident laser exposure on porosity characteristics and tensile performance of stainless steel 316L (SS316L) fabricated via laser powder bed fusion (L-PBF) was experimentally investigated. Miniature tensile specimens were fabricated using a TRUMPF TruPrint 2000 system under single-laser (0° and 45° hatch) and dual-laser (90° hatch with ~2 mm overlap) scan strategies, with the overlap region intentionally located at the center of the gauge section. X-ray computed tomography (XCT) was employed to characterize porosity distribution. Tensile testing revealed that single-laser 0° hatch produced the highest yield and ultimate tensile strengths, while the 45° hatch condition exhibited greater ductility at lower strength. Dual-laser 90° hatch samples maintained comparable ultimate strength but showed reduced yield strength and ductility, with premature failure linked to the coincident overlap region. These findings highlight the impact of scan strategy and laser overlap design on the mechanical performance of SS316L L-PBF components.

Keywords: laser powder bed fusion (L-PBF), X-ray CT, porosity analysis, dual L-PBF, coincident exposure, tensile properties

1. Introduction

Additive manufacturing (AM) of metals has gained increasing attention in both research and industry over the last decades and continues to expand rapidly with applications in aerospace, biomedical implants, construction, energy systems, and thermal management. Its popularity stems from the ability to fabricate complex geometries, reduce material waste, and enable design freedom beyond the limitations of conventional subtractive manufacturing. Within the landscape of metal AM technologies, including Directed Energy Deposition and Binder Jetting, Laser Powder Bed Fusion (L-PBF) has emerged as one of the most widely adopted processes due to its capability for high precision, fine feature resolution, and consistent part quality.

In L-PBF, a thin powder layer is distributed across the build area by a recoating mechanism, and a high-energy laser selectively melts the powder according to a predefined scanning pattern. The molten pool solidifies rapidly at cooling rates that can exceed 10^6 K/s [1], and this sequence repeats layer by layer until the full part is built. The rapid thermal cycling, repeated melting and solidification, and localized energy input inherent to this process strongly influence the resulting microstructure and defect distribution. As a result, the final properties of L-PBF parts are closely tied to the nature of laser–powder interaction and to the chosen process parameters [2], [3].

Porosity remains one of the most significant defects in L-PBF components, as pores can originate from incomplete fusion, keyholing, or entrapped gas during solidification [4]. The distribution, size, and morphology of pores affect local stress concentration, crack initiation, and ultimately the mechanical performance of the part. Alongside porosity, the microstructural characteristics such as grain orientation, texture, and substructure are highly sensitive to the applied scan strategies [5]. Variation in hatch orientation or laser exposure sequence has been shown to alter thermal gradients and solidification patterns, resulting in measurable differences in yield strength, ductility, and fractured behavior.

The transition from single-laser to multi-laser L-PBF systems has further amplified these considerations. While multi-laser platforms increase productivity by dividing the build area among multiple beams, they also introduce overlap regions where coincident laser exposures occur. These overlap zones are prone to process instabilities, heterogeneous microstructures, and localized porosity accumulation, which may degrade the mechanical reliability of printed components [6], [7]. Understanding the effects of these overlapping regions on part integrity is therefore essential for optimizing multi-laser build strategies and ensuring reproducibility at industrial scales [8], [9].

In this study, the influence of coincident laser exposure on the porosity distribution and tensile performance of L-PBF SS316L is systematically investigated. Miniature tensile coupons were produced under single-laser and dual-laser scan strategies, with overlapping was intentionally introduced at the gauge section. Porosity analysis was conducted using X-ray computed tomography, and tensile behavior was evaluated for each condition.

2. Experimental Methods

Gas-atomized MetcoAdd™ 316L-A stainless steel powder (Oerlikon) was used in this study. The nominal particle size distribution ranged from 15–45 μm with an apparent density above 4 g/cm^3 , consistent with high-quality feedstock. Specimens were fabricated using a TRUMPF TruPrint 2000 system equipped with dual 300 W fiber lasers operating at a wavelength of 1070 nm (Fig. 1). The system was operated using a nitrogen-purged environment to suppress oxidation. Major process parameters include: laser power = 113 W for each laser, scan speed = 1000 mm/s, vector distance = 0.08 mm, substrate preheat temperature = 200 $^{\circ}\text{C}$, and layer thickness = 20 μm . All of these process parameters were held constant across builds, with only the scan strategy varied.

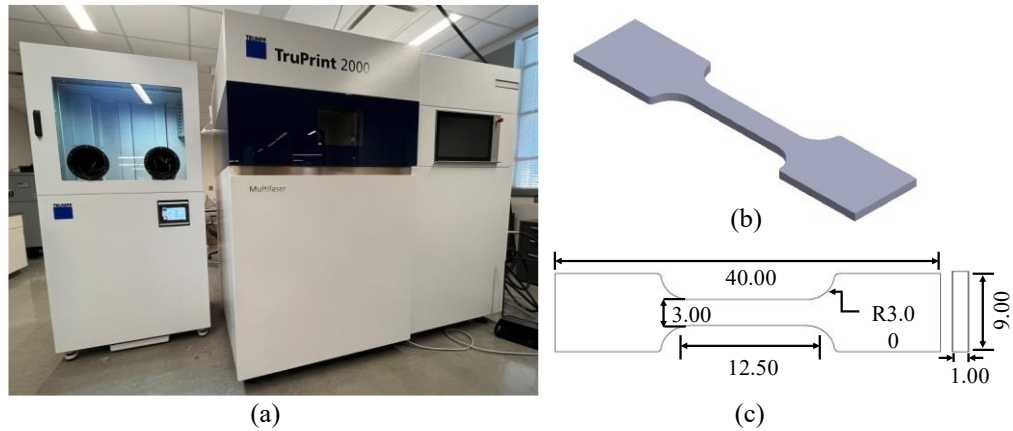


Figure 1: (a) TRUMPF TruPrint 2000 Dual L-PBF system. Miniature tensile coupon (b) CAD (c) detailed drawing.

Miniature tensile coupons were designed based on the ASTM SS-12.5 miniature tensile standard developed by Kolhatkar et al. [10]. The specimen geometry features a gauge section measuring 3 mm in width, 1 mm in thickness, and 12.5 mm in length, as illustrated in the CAD model and detailed drawing (Fig. 1(b & c)). This geometry has been validated for small AM coupons where full-sized standards are less practical.

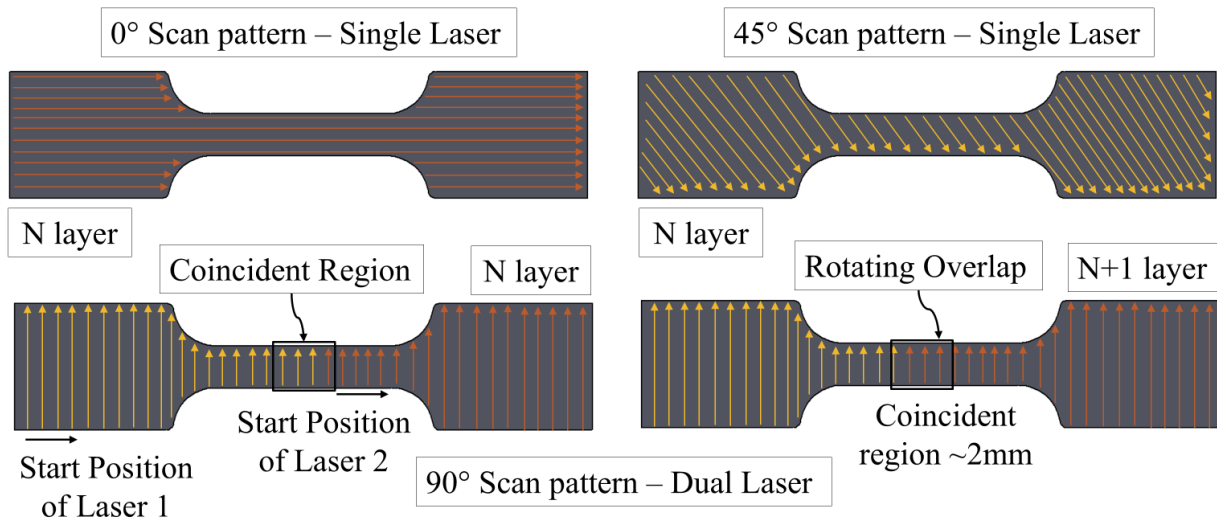


Figure 2: Schematic of applied scan strategies for dual L-PBF of tensile coupons.

Scan strategies were selected to contrast single-laser and dual-laser exposure modes (Fig. 2). For single-laser builds, linear hatches were applied at 0° and 45° orientations without layer-to-layer rotation. For the dual-laser case, a preset alternating strategy was employed in which each laser scanned perpendicular fields with a designed overlap placed at the specimen gauge center. The relative start and end positions of the two lasers were offset between layers, ensuring that the overlap zone did not repeat identically from layer to layer. This approach provided a controlled coincident region while avoiding excessive rescanning of the same area. After printing, the tensile

coupons were labeled as S1–S8 for the single-0° condition, S9–S13 for the single-45° condition, and M1–M8 for the dual-90° condition.

Mechanical testing was carried out on an MTS Landmark servohydraulic system. Testing was performed under displacement control at a crosshead speed of 1 mm/min, with data acquisition at 20 Hz. A total of five replicate specimens were tested for each scan strategy. As-built specimens were used directly, and wedge grips with alignment fixtures ensured consistent positioning during testing. Porosity was characterized by using a Zeiss Xradia 510 Versa X-ray computed tomography (XCT) system. For tensile specimens, a voxel size of $\sim 3.5 \mu\text{m}$ was selected to balance resolution with sample size, enabling full-gauge reconstructions of the tensile section ($\sim 77 \text{ mm}^3$) for three-dimensional visualization and quantification of pore distributions.

3. Results and Discussion

Miniature tensile coupons were fabricated, tested, characterized, and analyzed to identify process-property relationships. Figure 3(a) shows the tensile coupons printed while still attached to the 100-mm substrate. Coupons were oriented horizontally for printing to capture and exacerbate the dual laser movement across the gauge center during scanning. Volume support was included to reduce local heat accumulation associated with the 1 mm gauge thickness and to mitigate bending from residual stress after removal from the baseplate (i.e., substrate) by bench saw. A representative coupon after removal and surface finishing by milling is shown in Fig. 3(b).

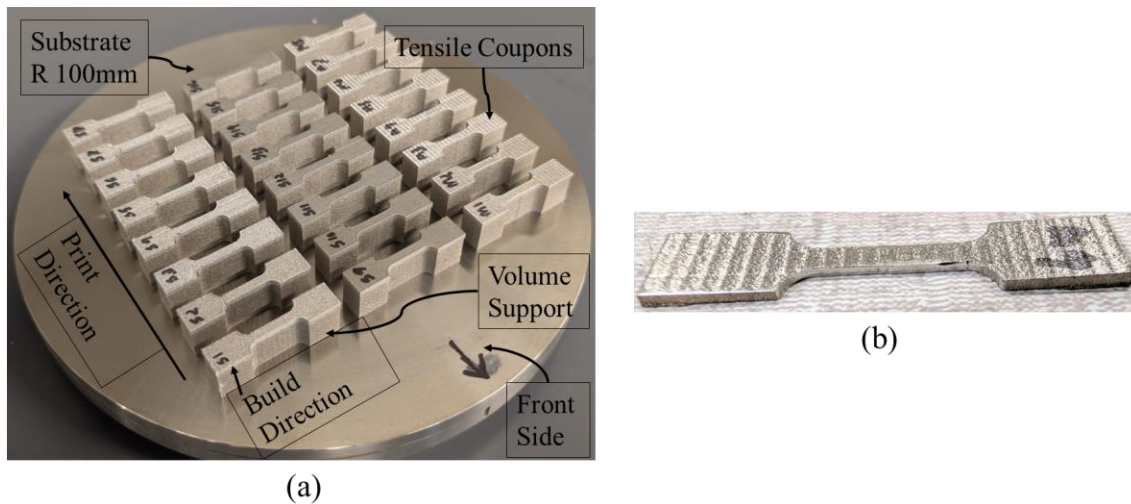


Figure 3: (a) Printed tensile coupons on the baseplate. (b) Removed sample (M4) from baseplate.

3.1 Porosity Characteristics

X-ray computed tomography (XCT) was used to quantify porosity distributions within the tensile gauge regions, with data post-processed in Dragonfly (Version 2024.1) software. Porosity was segmented in Dragonfly by thresholding low-density regions relative to the surrounding material, with parameters tuned to improve the accuracy of pore identification and quantification. All printed coupons exhibited high relative density, with global porosity levels below 0.8%. Three-dimensional pore reconstructions and representative pore size distributions are shown in Fig. 4(a) and Fig. 4(b), respectively, and the corresponding porosity statistics are summarized in Table 1.

Among the single-laser strategies, the single laser 0° (Fig. 4(a) – S5) exhibited the highest global porosity (~0.75%), dominated by fine pores below 10 μm. Among the single-laser strategies, the single laser 0° (Fig. 4(a) – S5) exhibited the highest global porosity (~0.75%), dominated by fine pores below 10 μm. This high density of small pores is consistent with the unidirectional scanning pattern, where melt tracks are exposed repeatedly along the same orientation, increasing the likelihood of pore entrapment (S5) [11]. The 45° single-laser condition (Fig. 4(a) – S13) showed the lowest porosity (~0.01%) and the smallest average pore size (~8.5 μm). Pores in this case were more spherical, indicating greater melt pool stability and more effective gas escape. The dual-90° condition (Fig. 4(a) – M5) had an intermediate porosity (~0.06%) but contained larger critical defects, including one exceeding ~677 μm found near the surface/contour of the part. These defects were less spherical compared to those in single-laser samples and represent the dominant feature of the porosity profile for this scan strategy.

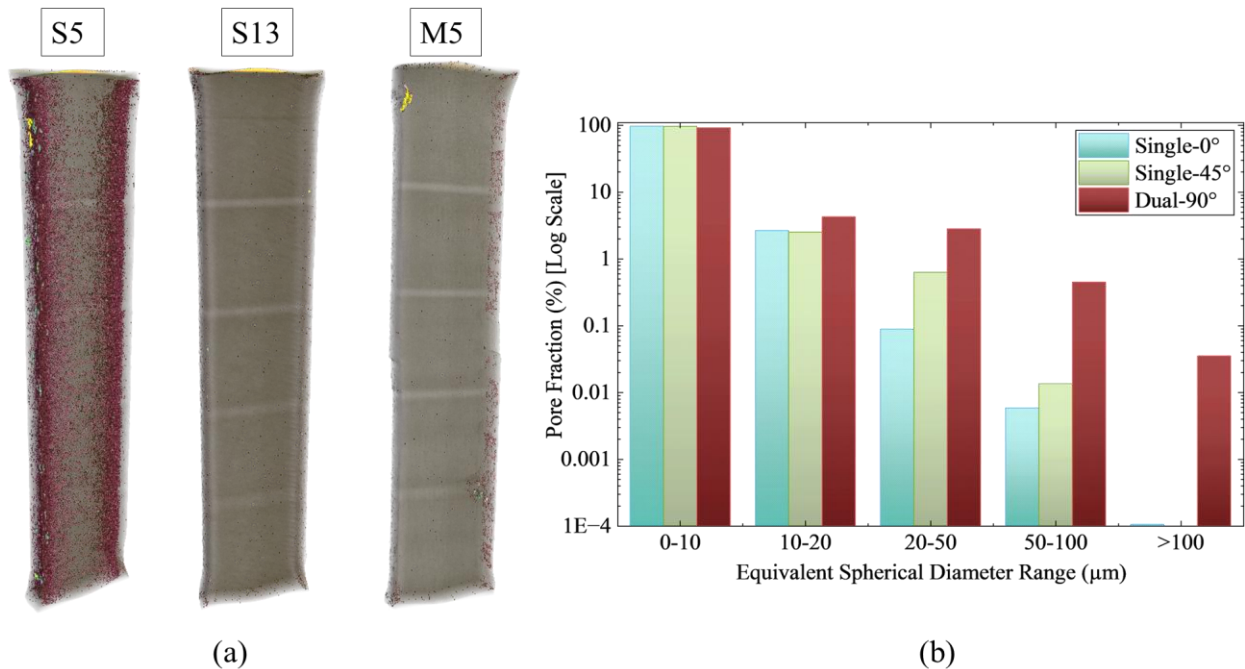


Figure 4: (a) Three-dimensional pore reconstructions of tensile coupons for single-0° (S5), single-45° (S13), and dual-90° (M5) scan strategies. (b) Equivalent spherical diameter distributions of pores for the three scan strategies on a logarithmic scale.

3.2 Tensile behavior

Fracture positions were found to vary with scan strategy (Fig. 5(b)). The dual 90° coupons fractured near the coincident region, while the single-laser coupons fractured farther from the gauge center, typically close to the fillet transition between the reduced gauge and the wider grip section. Stress–strain curves for each scan strategy are presented in Fig. 5(a), and the corresponding average properties are summarized in Table 1.

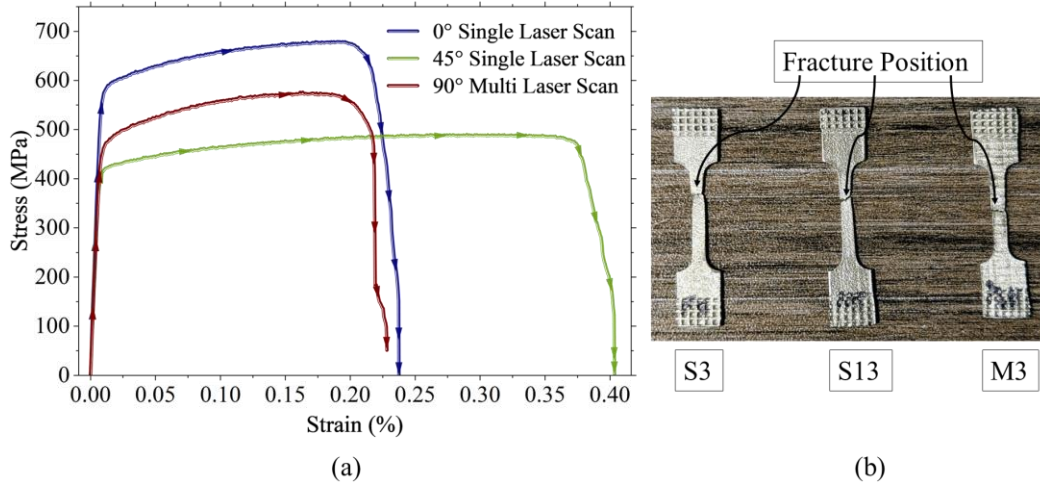


Figure 5: (a) Representative stress–strain curves and (b) fractured tensile coupons for single-0° (S3), single-45° (S13), and dual-90° (M3) samples.

The single 0° condition achieved the highest strength, with ultimate tensile strength (UTS) ~631 MPa and yield strength (YS) ~500 MPa (0.2% YS ~539 MPa), but with limited ductility of ~18%. The single 45° condition showed lower strength (UTS ~559 MPa, YS ~456 MPa, 0.2% YS ~474 MPa) but produced the greatest elongation of ~28%. The dual 90° condition retained UTS similar to the single 45° case (~565 MPa) but with reduced YS (~407 MPa; 0.2% YS ~453 MPa) and ductility (~18%). The Young’s modulus ranged between ~50–61 GPa, with minimal variation between scan strategies.

The observed differences in the mechanical properties can be explained by two main aspects. First, the scan strategies influenced thermal histories and melt pool development (and solidification). The straight scan lines in the single-0° condition likely promoted extended melt pools and more aligned columnar features, which have been reported in the literature to contribute to higher YS and UTS [12]. In contrast, the inclined single-45° strategy, with shorter exposure per track, resulted in comparatively lower strengths. The dual-90° strategy, incorporating rotating overlap in the coincident region, may have mitigated heat accumulation at the same location layer by layer, thereby retaining UTS.

Table 1: Summary of tensile properties (reported as mean ± SD for each scan strategy) and porosity characteristics obtained from XCT analysis. Porosity values are representative results from coupons S5 (single-0°), S13 (single-45°), and M5 (dual-90°).

Sample	UTS (MPa)	YS (MPa)	0.2% YS (MPa)	Young’s Modulus (GPa)	Ductility (%)	No. of Pores (N)	Global Porosity (%)	95th Eqv. Sph. Dia. (µm)	Critical Defect Size (Max. Feret, µm)	Critical Defect sphericity (φ)
Single Laser – 0°	630 ± 45.81	499.74 ± 43.43	538.73 ± 37.35	61.34 ± 4.34	18.44 ± 10.68	1,966,262	0.75	9.22	429.05	0.372

Single Laser – 45°	559 ± 63.31	455.80 ± 57.95	474.00 ± 51	49.72 ± 11.32	28.39 ± 10.25	22,202	0.01	8.48	126.53	0.65
Multi Laser – 90°	565 ± 24.59	407.40 ± 31.58	452.80 ± 24.09	51.49 ± 6.61	17.85 ± 3.02	14,226	0.06	14.07	677.1	0.254

Second, although the overall pore fractions do not fully align with mechanical performance trends, the pore size distribution and critical defect morphology offer better insight into the observed mechanical behavior. The single-0° condition exhibited the highest pore count, but most pores were very small and less spherical, supporting high YS and UTS while limiting ductility. The single-45° condition, with fewer pores and more spherical shapes, aligned with the greatest elongation. For the dual-90° condition, overall porosity was moderate, but the presence of large, irregular defects dominated mechanical behavior, reducing ductility. Notably, the critical defect size and morphology in the single-0° and dual-90° builds corresponded closely to the ductility outcomes. Additionally, all tensile tests were conducted on specimens oriented normal to the build direction, which has been associated with lower mechanical performance in prior studies [13], [14]. It should also be noted that surface roughness and the absence of EDM part removal could have influenced the measured properties.

4. Conclusions

In this study, the effect of scan strategy on the porosity and tensile properties of L-PBF SS316L was systematically investigated. The single-0° condition achieved the highest strength but introduced numerous fine pores that limited ductility. The single-45° condition minimized porosity and produced the most favorable balance between strength and elongation. The dual-90° condition maintained UTS but generated larger, irregular defects that reduced ductility and promoted earlier fracture initiation. Overall, the coincident region in dual-laser scanning is not inherently detrimental, and the rotating overlap may mitigate localized heat accumulation. However, consistent performance will require further optimization of scan parameters, supported by post-processing methods such as heat treatment or hot isostatic pressing.

Acknowledgments

The authors gratefully acknowledge the University of Missouri (MU) Materials Science & Engineering Institute (MUMSEI) for supporting this study. The authors also thank Mr. Christopher Strehl, Senior Research Specialist in the MU College of Engineering, for his assistance with tensile testing.

References

- [1] E. A. Lass *et al.*, “Formation of the Ni₃Nb δ -Phase in Stress-Relieved Inconel 625 Produced via Laser Powder-Bed Fusion Additive Manufacturing,” *Metall Mater Trans A Phys Metall Mater Sci*, vol. 48, no. 11, pp. 5547–5558, Nov. 2017, doi: 10.1007/s11661-017-4304-6.
- [2] B. P. Croom *et al.*, “Contributions of porosity and laser parameter drift to inter-build variation of mechanical properties in additively manufactured 316 L stainless steel,” *J Mater Process Technol*, vol. 317, p. 117998, 2023, doi: <https://doi.org/10.1016/j.jmatprotec.2023.117998>.

- [3] L. Afroz, M. Qian, J. Forsmark, Y. Li, M. Easton, and R. Das, "Fatigue life of laser powder bed fusion (L-PBF) AlSi10Mg alloy: effects of surface roughness and porosity," *Progress in Additive Manufacturing*, 2024, doi: 10.1007/s40964-024-00759-x.
- [4] M. Ben Slama, S. Chatti, and L. Kolsi, "Effect of processing parameters on porosity defects during SLM: a DOE-FEM approach," *Welding in the World*, vol. 67, no. 9, pp. 2201–2213, 2023, doi: 10.1007/s40194-023-01566-8.
- [5] O. O. Salman *et al.*, "Impact of the scanning strategy on the mechanical behavior of 316L steel synthesized by selective laser melting," *J Manuf Process*, vol. 45, pp. 255–261, 2019, doi: <https://doi.org/10.1016/j.jmapro.2019.07.010>.
- [6] Y. Xie *et al.*, "The role of overlap region width in multi-laser powder bed fusion of Hastelloy X superalloy," *Virtual Phys Prototyp*, vol. 18, no. 1, 2023, doi: 10.1080/17452759.2022.2142802.
- [7] Z. Liu, C. Song, X. Han, Y. Xiao, K. Liu, and Y. Yang, "Effect of dual-laser powder bed fusion on surface quality, internal defects and properties of 316L stainless steel," *Journal of Materials Research and Technology*, vol. 27, pp. 5681–5691, Nov. 2023, doi: 10.1016/j.jmrt.2023.10.221.
- [8] K. Wei *et al.*, "Multi-laser powder bed fusion of Ti–6Al–4V alloy: Defect, microstructure, and mechanical property of overlap region," *Materials Science and Engineering: A*, vol. 802, Jan. 2021, doi: 10.1016/j.msea.2020.140644.
- [9] C. Zhang, H. Zhu, Z. Hu, L. Zhang, and X. Zeng, "A comparative study on single-laser and multi-laser selective laser melting AlSi10Mg: defects, microstructure and mechanical properties," *Materials Science and Engineering: A*, vol. 746, pp. 416–423, 2019, doi: <https://doi.org/10.1016/j.msea.2019.01.024>.
- [10] A. Kolhatkar, V. Karthik, G. M. S. K. Chaitanya, A. Kumar, and D. Ramchandran, "Development and validation of a miniature tensile specimen for determination of mechanical properties," *J Test Eval*, vol. 47, no. 5, Sep. 2019, doi: 10.1520/JTE20180294.
- [11] A. Kudzal *et al.*, "Effect of scan pattern on the microstructure and mechanical properties of Powder Bed Fusion additive manufactured 17-4 stainless steel," *Mater Des*, vol. 133, pp. 205–215, 2017, doi: <https://doi.org/10.1016/j.matdes.2017.07.047>.
- [12] J. J. Marattukalam *et al.*, "The effect of laser scanning strategies on texture, mechanical properties, and site-specific grain orientation in selective laser melted 316L SS," *Mater Des*, vol. 193, p. 108852, 2020, doi: <https://doi.org/10.1016/j.matdes.2020.108852>.
- [13] K. Dai *et al.*, "Tailoring the microstructure and mechanical properties for Hastelloy X alloy by laser powder bed fusion via scanning strategy," *Mater Des*, vol. 235, p. 112386, 2023, doi: <https://doi.org/10.1016/j.matdes.2023.112386>.
- [14] Y. C. Wang, L. M. Lei, L. Shi, H. Y. Wan, F. Liang, and G. P. Zhang, "Scanning strategy dependent tensile properties of selective laser melted GH4169," *Materials Science and Engineering: A*, vol. 788, p. 139616, 2020, doi: <https://doi.org/10.1016/j.msea.2020.139616>.